Title: Comparison of Rhesus and Cynomolgus macaques as an authentic model for COVID-19.

Authors: Francisco J. Salguero[1], Andrew D. White[1], Gillian S. Slack[1], Susan A. Fotheringham[1], Kevin R. Bewley[1], Karen E. Gooch[1], Stephanie Longet[1], Holly E. Humphries[1], Robert J. Watson[1], Laura Hunter[1], Kathryn A. Ryan[1], Yper Hall[1], Laura Sibley[1], Charlotte Sarfas[1], Lauren Allen[1], Marilyn Aram[1], Emily Brunt[1], Phillip Brown[1], Karen R. Buttigieg[1], Breeze E. Cavell[1], Rebecca Cobb[1], Naomi S. Coombes[1], Owen Daykin-Pont[1], Michael J. Elmore[1], Konstantinos Gkolfinos[1], Kerry J. Godwin[1], Jade Gouriet[1], Rachel Halkerston[1], Debbie J. Harris[1], Thomas Hender[1], Catherine M.K. Ho[1], Chelsea L. Kennard[1], Daniel Knott[1], Stephanie Leung[1], Vanessa Lucas[1], Adam Mabbutt[1], Alexandra L. Morrison[1], Didier Ngabo[1], Jemma Paterson[1], Elizabeth J. Penn[1], Steve Pullan[1] ,Irene Taylor[1], Tom Tipton[1], Stephen Thomas[1], Julia A. Tree[1], Carrie Turner[1], Nadina Wand[1], Nathan R. Wiblin[1], Sue Charlton[1], Bassam Hallis[1], Geoffrey Pearson[1], Emma L. Rayner[1], Andrew G. Nicholson[2], Simon G. Funnell[1], Mike J. Dennis[1], Fergus V. Gleeson[3], Sally Sharpe[1], Miles W. Carroll[1,*].

Affiliations:

[1]National Infection Service, Public Health England (PHE), Porton Down, Salisbury, Wiltshire, United Kingdom. SP4 0JG.

[2]Royal Brompton and Harefield NHS Foundation Trust, and National Heart and Lung Institute, Imperial College, London

[3]Department of Oncology, Oxford University, Oxford, UK.

***Corresponding author**

Professor Miles Carroll. National Infection Service. Public Health England. Porton Down, Salisbury, Wiltshire, SP4 0GJ. Email: miles.carroll@phe.gov.uk. Telephone: 01980 612100

Short title: COVID-19 infection in Rhesus and Cynomolgus macaques

ABSTRACT

A novel coronavirus, SARS-CoV-2, has been identified as the causative agent of the current COVID-19 pandemic. Animal models, and in particular non-human primates, are essential to understand the pathogenesis of emerging diseases and to the safety and efficacy of novel vaccines and therapeutics. Here, we show that SARS-CoV-2 replicates in the upper and lower respiratory tract and causes pulmonary lesions in both rhesus and cynomolgus macaques, resembling the mild clinical cases of COVID-19 in humans. Immune responses against SARS-CoV-2 were also similar in both species and equivalent to those reported in milder infections and convalescent human patients. Importantly, we have devised a new method for lung histopathology scoring that will provide a metric to enable clearer decision making for this key endpoint. In contrast to prior publications, in which rhesus are accepted to be the optimal study species, we provide convincing evidence that both macaque species authentically represent mild to moderate forms of COVID-19 observed in the majority of the human population and both species should be used to evaluate the safety and efficacy of novel and repurposed interventions against SARS-CoV-2. Accessing cynomolgus macaques will greatly alleviate the pressures on current rhesus stocks.

INTRODUCTION

A novel acute respiratory syndrome, now called Coronavirus disease-19 (COVID-19) was first reported in Wuhan, China in December 2019. The genetic sequence of the causative agent was found to have similarity with two highly pathogenic respiratory beta Coronaviruses, SARS [1] and MERS [2], and was later called SARS-CoV-2 [3]. It has currently infected >21 million individuals resulting in >750,000 deaths [4]. Among the clinical and pathological signs of SARS-CoV-2 infection in humans, pneumonia accompanied by respiratory distress seem to be the most clinically relevant [5,6].

The development of animal models that replicate human disease is a crucial step in the study of pathogenesis and transmission, in addition to the assessment of the safety and efficacy of candidate vaccines and therapeutics. Due to their obvious physiological similarities to humans, non-human primates (NHPs), such as macaques, have long been recognised as the most clinically relevant animal for development of *in vivo* models of human disease. Prior NHP models developed for SARS and MERS have shown respiratory induced pathology with similar features as those seen in humans, including diffuse alveolar damage. For SARS, though rhesus macaques became the preferred species, the literature suggests there is no significant difference in susceptibility of cynomolgus (*Macaca fascicularis*) or rhesus macaques (*Macaca mulatta*) to infection, virus replication and pathology [7-10]. Recent studies have shown that rhesus macaques [11,12] and cynomolgus macaques [13] can be infected by SARS-CoV-2 and the disease course resembles some features of human COVID-19 infection. Rhesus macaques appear to display more extensive lung pathology and clinical signs, however a direct comparison of species, based on these studies, is not possible because different strains of virus, dose and route of administration have been used. There is an accepted preference to use rhesus macaques for the assessment of COVID-19 vaccine and therapeutics, based on the limited number of studies that have been performed. A head-to-head comparison of rhesus versus cynomolgus macaques, under the same experimental conditions, is urgently required as there are now acute pressures on rhesus stocks that will impact on the ability to perform safety and efficacy studies on new vaccines and therapeutics.

This unique study aims to evaluate the outcome of exposure to SARS-CoV-2 in a head to head comparison of two macaque species: rhesus macaque (Indian genotype) and cynomolgus macaque (Mauritian genotype) exposed to the same well characterized strain of challenge virus. The resulting disease course in each species was closely compared for the first time.

Similar to recent NHP studies, a dose of $5x10^6$ pfu of SARS-CoV-2/Victoria/01/2020 [14], was delivered via the intranasal (IN) and intratracheal (IT) route to groups of each species comprising six animals. Sequential body fluid sampling and culls (at days 4/5, 14/15 and 18/19) were performed to support a comprehensive comparative assessment of clinical signs, pathology, virology and immunology.

RESULTS

Clinical signs and in-life imaging by CT scan

Six rhesus macaques of Indian genotype and six cynomolgus macaques of Mauritian genotype were obtained from established UK Government breeding colonies. Study groups comprised three males and three females of each species and all were adults aged two to four years with body weights ranging between 2.89 - 4.85kg at time of challenge. Animals were challenged with a total of $5x10^6$ pfu of SARS-CoV-2/Victoria/01/2020 administered in volumes of 2 ml by the intratracheal route (using a bronchoscope for accurate placement right above the carinal bifurcation) and 1 ml by the intranasal route (0.5 ml in each nostril). Whole genome sequencing of the viral challenge stock, used in this study (Passage 3), confirmed there were no significant changes following passage in Vero/hSLAM cells, compared to the original isolate (Passage 1).

No significant weight loss or changes in body temperature were observed throughout the experiment. Adverse clinical signs were not recorded for any animal despite frequent monitoring during the study period.

Images from CT scans collected 18 days after challenge from two rhesus and two cynomolgus macaques, were examined by an expert thoracic radiologist with experience of non-human primate prior CT interpretation and human COVID-19 CT features, blinded to the clinical status. Pulmonary abnormalities that involved less than 25% of the lung and reflected those characteristic of SARS-CoV-2 infection in humans, were identified in one rhesus macaque and both cynomolgus macaques (Figure 1). Ground glass opacity was observed in all three macaques showing abnormal lung structure, with peripheral consolidation also seen in one cynomolgus macaque. Abnormalities occurred in the peripheral two thirds of the middle and lower lung lobes in the two cynomolgus macaques and in a random pattern in the upper, middle and lower lobes of the rhesus macaque. Pulmonary emboli were not identified in any of the subjects.

Viral load in clinical samples

Viral load in the upper respiratory tract (URT) (nasal washes and throat swabs), gastrointestinal tract (rectal swabs) and in systemic samples (EDTA blood) was assessed by RT-qPCR at regular intervals throughout the study, and in bronchioalveolar lavage (BAL) collected at necropsy (Figure 2). High levels of viral RNA (>10^6 cDNA copies/ml) were detected in nasal wash samples collected from both species one day post challenge (dpc). In rhesus macaques, viral RNA in nasal washes peaked at two dpc at $6.9 \pm 2.3 \times 10^7$ cDNA copies/ml and levels remained between 2.9×10^5 and 4.8×10^7 cDNA copies/ml until eleven dpc, before decreasing to $\leq 1.8 \times 10^4$ cDNA copies/ml by 18 dpc. Cynomolgus macaques displayed a similar pattern of viral RNA burden in nasal wash samples with peak levels detected at three dpc. However, levels later in infection remained higher with titres of 2.0×10^6 cDNA copies/ml at 15 dpc and 1.6×10^5 cDNA copies/ml at 19 dpc (Figure 2A).

Viral load in throat swabs largely mirrored that in nasal washes with peak levels early in infection, although, overall titres were lower. This was most notable at two dpc (Figure 2B). In rhesus macaques, viral RNA was detected above the lower limit of quantification (LLOQ - 2.66×10^3 copies/ml) in all but one animal between one and three dpc and remained $\geq 1.5 \times 10^4$ copies/ml for all animals between four and nine dpc before falling and remaining below the assay's lower limit of detection (LLOD) from eleven dpc to 18 dpc. Throat swabs from cynomolgus macaques contained higher levels of viral RNA early in infection (one to three dpc) and remained ≥4.5 x 10^4 copies/ml for all animals between four and nine dpc.

Viral load in BAL samples echoed URT samples, with high (≥9.8 x 10^6 copies/ml) levels in both species at four and five dpc, dropping to ≤2.4 x 10^4 copies/ml and ≤1.9 x 10^4 copies/ml at 14 dpc and 15 dpc in rhesus and cynomolgus macaques, respectively (Fig. 2C).

Virus shedding from the gastrointestinal tract was assessed by RT-qPCR performed on rectal swab samples. In rhesus macaques, low levels of viral RNA were detected from one dpc to nine dpc. In cynomolgus macaques, viral RNA was similarly detected at a low level in rectal swabs from one dpc to nine dpc. However viral RNA levels above the LLOQ were detected at both three dpc and five dpc in cynomolgus macaques in comparison to two dpc and three dpc in rhesus macaques (Figure 2D). Viral RNA was detected at only two timepoints after challenge in whole blood samples and remained below the LLOQ throughout the study (Figure 2E). In rhesus macaques, viral RNA was detected in one animal at three dpc, whilst in cynomolgus macaques, viral RNA was detected in two animals at six dpc.

Samples collected from the upper respiratory tract at each study time point were evaluated using a Vero cell-based plaque assay for the presence of viable virus. Viable virus was successfully recovered from two of the six rhesus macaques and three of the six cynomolgus macaques on the first occasion of sampling (one to three dpc). In all cases, recovery was below 100 pfu/mL based on a figure of under 10 plaques in a single well. Virus was not recovered from any nasal wash samples collected from four dpc onwards.

Pathological changes

Gross pathological changes were found in the lungs of all animals from both species and sexes euthanised 4/5 days after challenge and consisted of multiple areas of mild to moderate consolidation distributed in cranial and caudal lobes. At 14/15 and 18/19 dpc, only small areas of consolidation were observed. Macroscopic remarkable changes were not observed in any other organ analysed in this study at any time point.

Histological changes in the lungs of all twelve animals from both species, consistent with infection with SARS-CoV-2, were observed. The changes were most prominent at 4/5 dpc and thereafter were less severe, indicating resolution of the more acute changes observed at early time points.

4/5 days after challenge, the lung parenchyma in the cynomolgus macaques was comprised of multifocal to coalescing areas of pneumonia, surrounded by unaffected parenchyma. Overall, diffuse alveolar damage (DAD) was a prominent feature in the affected areas, characterised by individual, shrunken, eosinophilic cells in alveolar walls, with pyknotic or karyorrhectic nuclei (Figure 3A). In these areas, alveolar spaces were often obliterated by collapse of the thickened and damaged alveolar walls which contained mixed inflammatory cells (Figure 3A); or had obvious, alveolar type 2 pneumocyte hyperplasia (alveolar epithelialisation), as well as expanded alveolar spaces (Figure 3B). Alveolar spaces were expanded and filled with fibrillar to homogenous, eosinophilic, proteinaceous fluid (alveolar oedema) (Figure 3A), admixed with fibrin, polymorph neutrophils (PMNs), enlarged alveolar macrophages and other round cells (possibly detached type 2 pneumocytes). In distal bronchioles and bronchiolo-alveolar junctions, degeneration and sloughing of epithelial cells was present, with areas of attenuation and foci of plump, type 2 pneumocytes representing regeneration.

In the larger airways occasional, focal, epithelial degeneration and sloughing was observed in the bronchial epithelium, with evidence of regeneration, characterised by small, basophilic epithelial cells. Low numbers of mixed inflammatory cells, comprising PMNs, lymphoid cells, and occasional eosinophils, infiltrated bronchial and bronchiolar walls. In the lumen of some airways, fibrillar, eosinophilic material (mucus), admixed with degenerative cells, mainly PMNs and epithelial cells, was seen. Occasionally, multinucleated cells, characterised as large, irregularly shaped cells with prominent, eosinophilic cytoplasm and multiple round nuclei, resembling syncytial cells (Figure 3B, inset) were observed.

Pathological changes consistent with those described for cynomolgus macaques were present in the lungs of rhesus macaques. In the parenchyma, multifocal expansion and infiltration of alveolar walls by inflammatory cells was noted (Figure 3E). Furthermore, in these areas, DAD was observed with patchy alveolar oedema and hyperplasia of alveolar macrophages (Figure 3F). In the bronchi and bronchioles, similar changes to those described for cynomolgus macaques were seen.

Presence of viral RNA was observed in the lungs from all animals at 4/5 dpc by *in situ* hybridisation. Prominent staining of small foci of cells containing SARS-CoV-2 viral RNA, was observed within the alveolar walls, concomitant with microscopic changes in cynomolgus macaques (Figure 3C). Staining was not seen in cells or fluid within the alveolar spaces. Positive cells were also observed rarely in the bronchus-associated lymphoid tissue (BALT) (Figure 3C, insert). Abundant numbers of cells expressing IL-6 mRNA were observed within the pulmonary lesions (Figure 3D), with only few positive scattered cells in the healthy parenchyma.

Small foci of cells staining positive for viral RNA were observed at a low frequency in the rhesus macaques within the alveolar walls and interalveolar septa of both animals at 4/5 dpc, concomitant with microscopic changes (Figure 3G). IL-6 mRNA was also abundant within the lesions (Figure 3H).

Changes were less severe in all four animals examined at 14/15 dpc. In the cynomolgus macaques, patchy infiltration of mainly mononuclear cells in the alveolar walls, with occasional similar cells within alveolar spaces, and parenchymal collapse, were seen (Figure 3I). Mononuclear cells, primarily lymphocytes also were noted surrounding and infiltrating the walls of blood vessels and airways (Figure 3J). An increased prominence of bronchial-associated lymphoid tissue (BALT) was noted. In the lungs of rhesus macaques, changes in the alveoli and BALT were similar in appearance and frequency to those described in the cynomolgus macaques, and perivascular lymphocytic cuffing of small vessels, characterised by concentric infiltrates of mononuclear cells, was also seen occasionally (Figure 3K and 3L).

Viral RNA was detected in only a few individual cells in both groups of animals at 14/15 dpc (Figure 3J, insert; 3L, insert). By day 18/19, the changes were similar but less frequent to those described at day 14/15 in all four animals and viral RNA was not detected by ISH.

In summary, using the histopathology scoring system developed here, the scores were higher in both macaque species at 4/5 dpc compared to 14/15 and 18/19dpc, mostly due to higher scores in the alveolar damage parameters observed at the early time point (Figure 4A).

Overall, there was a high presence of viral RNA at 4/5 dpc which was more pronounced in the cynomolgus macaques, in contrast only very few positive cells were observed at 14/15 dpc and none at 18/19 dpc. (Figure 4B). A similar trend was observed in the presence of IL-6 mRNA with a higher amount at 4/5 dpc, which was slightly more pronounced in cynomolgus macaques, and lower expression at 14/15 dpc (Figure 4C).

Viral RNA was observed in scattered epithelial cells in areas of the upper respiratory tract (nasal cavity, larynx and trachea) of all animals at 4/5 dpc, and not associated to any remarkable lesion.

In the liver, microvesicular, centrilobular vacuolation, consistent with glycogen, together with, small, random, foci of lymphoplasmacytic cell infiltration were noted rarely (data not shown). This is considered to represent a mild, frequently observed background lesion. Remarkable changes were not observed in any other tissue. Viral

RNA staining was seen only at 4/5 dpc, in occasional, absorbing epithelial and goblet cells in the small and large intestine. It was not observed in any other tissue examined.

Antibody responses to SARS-CoV-2 infection

Low levels of neutralising antibody were detected by plaque reduction neutralisation test (PRNT) assay in both cynomolgus and rhesus macaques for the first eight to nine days post challenge. From day eleven or twelve, both species showed high neutralising antibody titres which continued at the later time point (14 to 19 dpc). The neutralisation titres at the later time points were generally higher in the cynomolgus macaques, although greater variability in titres between different animals was seen for this species (Figure 5).

Seroconversion to viral antigens Spike trimer, Receptor Binding Domain (RBD) and Nucleoprotein were evaluated by ELISA following infection. Specific antibodies against SARS-CoV-2 were detected in serum collected from both rhesus and cynomolgus macaques from eight to nine dpc onwards (Figure 6).

Frequency of Antigen-Specific IFN-γ Secreting Cells Measured by ELISpot

Cellular immune responses induced by SARS-CoV-2 challenge were measured in peripheral blood mononuclear cells (PBMCs) using an *ex vivo* IFN-γ ELISpot assay and compared to responses measured in uninfected (naïve) age and species matched control animals (Figure 7). Interrogation of IFN-γ spot forming units (SFU) measured in response to stimulation with overlapping 15-mer spike protein peptide pools indicated that peptides spanning the breadth of the SARS-CoV-2 spike protein sequence induced cellular immune responses in infected cynomolgus macaques; whereas, peptide pool (PP) sequences 2-4 and 8 were most immunogenic in rhesus macaques (Figure 7A-B).

In rhesus macaques, the IFN-γ SFU measured following stimulation with spike protein peptide megapools (MP) 1-3 did not differ significantly between animals euthanised at either the day 4-5 (early) or the day 14-19 (late) post-infection time-point in comparison to SFU frequencies measured in the naïve control animals. However, comparison of the summed MP 1-3-specific response indicated that significantly higher SFU frequencies were present in the animals euthanised at the later time-point ($P = 0.01$) (Figure 7C). By contrast, spike protein MP1-, MP2, and summed MP-specific responses measured in cynomolgus macaques were all significantly higher than in naïve control animals at the later post-infection time-point ($p = 0.03$, $p = 0.01$, $p = 0.01$) (Figure 7D).

In general, there was a trend for spike protein peptide-specific IFN-γ SFU frequencies measured in PBMC samples collected from cynomolgus macaques to be greater than those detected in rhesus macaques, although these differences did not reach statistical significance.

Spike peptide-specific IFN-γ SFU frequencies measured in mononuclear cells isolated from lung and spleen samples revealed a trend for local cellular immune responses to be greatest in the animals euthanised at the day 14 to19 post infection time point, but also that there was substantial variability within the groups at this stage of infection (Figure 7E).

Composition and functional profile of the cell mediated immune response. To explore changes in the composition of the cellular immune compartment following SARS-CoV-2 infection, immunophenotyping flow cytometry assays were applied to PBMCs and lung MNC samples collected at necropsy and from PBMCs collected from age and species matched uninfected (naïve) animals. Comparison of CD4+ and CD8+ T-cell frequencies indicated that the proportion of CD8+ T-cells was greater in cynomolgus macaques prior to, and also after infection when the frequency of the CD4+ subset increased but remained secondary to the CD8+ population in peripheral blood and lung MNC (Figure 7F). Similarly, the frequency of γδ T-cells in peripheral blood was higher in cynomolgus macaques but remained consistent following infection, whereas γδ T-cell frequencies appeared more variable in the lung MNC samples collected from animals euthanised at the early and late post infection time point (Figure 7G-H). Monocyte subtypes were characterised as classical, non-classical or intermediate by expression of CD14+ and CD16+. This revealed an increased frequency of ‘transitional’ CD14+ CD16+ and ‘non-classical’ CD14- CD16+ monocyte subsets in PBMCs collected at the later post-infection time point in both rhesus and cynomolgus species. In contrast, the immunomodulatory non-classical monocyte population was more abundant in lung tissue samples collected from rhesus macaques euthanised early after infection in comparison to the later time points or to cynomolgus macaques (Figure 7I). Cytotoxic and immunomodulatory natural killer (NK) cell populations were identified within the CD3-, CD159a+ lymphocyte population based on the expression on CD16 and CD56, respectively.

Immunomodulatory (CD56+) NK cell populations were detected at higher frequency in the lung and PBMC of infected macaques in comparison to naïve control animals, indicating a potential proinflammatory role for this innate lymphoid cell subset in SARS-CoV-2 infection (Figure 7J).

To explore the functional profile of T-cell populations, PBMCs were stimulated with peptide pools spanning the SARS-CoV-2 membrane (M), nucleocapsid (N) or spike (S) proteins, and the production of the cytokines IFN-γ, IL-2, TNF-α, IL-17 and GM-CSF along with the activation marker CD69 and degranulation marker CD107a measured by intracellular cytokine staining. Cytokine producing CD4 and CD8 T-cells were detected in both rhesus and cynomolgus macaques in response to stimulation with M, N and S peptide pools. Proinflammatory (IFN-γ or GM-CSF producing) T-cells were primarily detected at the later post-challenge time point, although low frequencies of IL-2 producing CD8+ cells were detected in PBMC samples collected from cynomolgus macaques in the early post-challenge samples (Figure 7K). The frequency of Th17 and TNF-α expressing cells differed between the species with IL-17 producing CD4 and CD8 T-cells more prevalent in rhesus macaques, whereas TNFα expression was detected more frequently in cynomolgus macaques. Similarly, cytokine production measured in the γδ T-cell population indicated a trend for greater IL-17 production in PBMCs isolated from rhesus macaques, although low frequencies of IFN-γ and IL-17 producing γδ T-cells were also detected in cynomolgus macaques euthanised at the early post-infection time point indicating that unconventional T-cell populations play a role in the early immune response to SARS-CoV-2 infection (Figure 7L). Peptide-specific expression of the degranulation marker CD107a was assessed as a measure of cell mediated cytotoxicity. CD107a was detected on CD8 and γδ T-cells in both rhesus and cynomolgus macaques, was most potently induced by stimulation with the M protein peptide pool and detected at higher frequency in cynomolgus macaques at the early post infection time points (Figure 7M-N). In addition to the above functional parameters, antigen-specific expression of the activation marker CD69 was assessed to provide a measure of the overall activation status and SARS-CoV-2 antigen-reactogenicity of T-cell subsets following infection. In general, CD69 expression on CD4, CD8 and γδ T-cell populations was higher at the later post infection timepoints (Figure 7K-L) and expression levels agreed with the detection of cytokine production in the corresponding T-cell subsets. However, instances of CD69 expression were also apparent in M, N and S peptide stimulated samples, in which there was an absence of cytokine or degranulation marker detection, indicating that these activated cells may have exerted antigen-specific functions outside of the parameters measured by our ICS assay.

DISCUSSION

We have shown for the first time in a head to head comparison that the consequences of challenge with SARS-CoV-2 in rhesus and cynomolgus macaques are similar and in line with outcomes described in studies conducted individually in either, rhesus [11,12,15,16] or cynomolgus macaques [13,17].

The clinical manifestations in human COVID-19 patients range from asymptomatic to severe [18-20]. In our study, we have observed that SARS-CoV-2 induced features characteristic of COVID-19 identified on CT scans in the absence of clinical signs in both rhesus and cynomolgus macaques. The lack of clinical signs observed agrees with other reports that used the IN and IT routes of challenge delivery [11,13,15,17]. The slightly increased levels of clinical changes previously described in rhesus [12,21,22] may be due to the use of the ocular and oral routes in addition to IN and IT for challenge and the potential impact of additional in-life sampling. CT provided the only clinical measure that identified abnormalities *in vivo* consistent with COVID-19 and is therefore a critical tool for evaluation of disease burden following experimental infection. Features characteristic of COVID-19 in human patients, such as ground glass opacity, consolidation and crazy paving were identified on CT scans collected from both SARS-CoV-2 challenged rhesus and cynomolgus macaques in line with reports from studies describing SARS-CoV-2 infection in either, rhesus [21], or cynomolgus macaques [17] supporting a role for both species as models of human SARS-CoV-2 induced disease.

The pattern of viral shedding from the URT (peak day one to three with subsequent decline to undetectable), intermittent low recovery from the gastrointestinal tract and absence of detection in the blood described across both species is similarly to what is observed in humans with asymptomatic/mild COVID-19 (shedding without clinical signs and/or after resolution of clinical course) and reflect previous reports of SARS-CoV-2 infection in rhesus [11,12,15,16] and cynomolgus macaques [13,17]. Similar to these studies, virus shed from the URT was detected by RT-qPCR very shortly after challenge, which could suggest the presence of residual challenge material rather than shedding of newly replicated virus resulting from infection. However, similar to Rockx et al., 2020, live virus was also detected, albeit at low levels, early after challenge which suggests some level of new virus replication which is also supported by the level of virus detected using RNA probes conducted on samples collected from animals euthanised 4/5 dpc (*13*).

Histopathological changes were comparable in both animal species, and closely resembled that seen in human cases following a mild/moderate clinical course. Typical changes of acute respiratory distress syndrome (ARDS) were observed, with DAD and alveolar hyperplasia seen on microscopy together with interstitial lymphoid infiltrates, focally showing perivascular cuffing. These histopathological lesions are compatible to those observed in human patients, although some features seen in humans, such as thromboembolic changes, were not present in the macaques [23]. The pathology at 14/15 and 18/19 dpc showed signs of resolution with some focal alveolar hyperplasia. We have described here a histopathology scoring system that allow us to quantify the severity of lesions in the airways and parenchyma of lung tissue sections from SARS-CoV-2 infected macaques. This system might prove to be very useful to compare quantitatively the lung histopathology observed in new vaccine and therapeutic trials.

We have also described herein an upregulation of local interleukin-6 production within the pulmonary lesions at the early time points of the infection in both species. The induction of a proinflammatory cytokine storm has been described in human COVID-19 patients, with IL-6 levels significantly elevated and associated with the disease severity [24,25].

The development of neutralising titres of specific antibodies is important for the control of infection and viral transmission and is a commonly reported feature in COVID-19 patients, although neutralising antibody alone is not considered sufficient for protection against severe disease [26]. IgG seroconversion occurred in both macaque species from days 8-9 post infection and therefore follows a similar kinetic to serology profiles measured in COVID-19 patients [27], indicating that both species offer representative models for the investigation of SARS-CoV-2 related humoral immunity.

In keeping with the generally mild pathology and limited evidence of viral replication or persistence reported in both macaque species, we detected little evidence in cellular immune profiles of the immune dysregulation associated with severe COVID-19 disease in humans [28]. Immunological features were more typical of those reported in milder infections and convalescent patients and included changes in the frequency of CD4 and CD8 T-cell populations [29] as well as increased frequencies of immunomodulatory NK [30] and monocyte subsets [31].

The role of T-cells in SARS-CoV-2 immunity is not fully defined, although, it is clear that CD4 and CD8 memory T-cells are present in COVID-19 convalescent patients and those previously exposed to related coronaviruses [32]. CD4 T-cell dependent mechanisms of protection have been demonstrated in small animal models of SARS-CoV infection [33], T-cells are likely to play an important role in the development of neutralising antibodies [34] and the clearance of infection through cell mediated cytotoxicity [26]. Our findings confirm that pro-inflammatory and cytotoxic T-cells are induced by SARS-CoV-2 infection in both rhesus and cynomolgus macaques to a similar extent, and that there is T-cell reactogenicity in both species to all three of the SARS-CoV-2 antigens included in our assays. This included the detection of antigen-specific immune responses directed toward peptide-epitopes spanning the S protein sequence, an antigen incorporated into several of the novel vaccine candidates currently under investigation [35], thus demonstrating the value of the macaque model for immunogenicity testing of novel SARS-CoV-2 vaccine constructs. Additionally, in a comparative study of colonisation of NHPs by group A *Steptococcus pyogenes* it was reported that cynomolgus developed a stronger antibody response compared to rhesus macaques [36], a trend that we also observed.

Our results demonstrate that both species provide authentic models of SARS-CoV-2 infection, that reflect upper and lower respiratory tract infection resulting in a lung injury, repair and resolution picture typical for milder forms of COVID-19 disease in humans. Both macaque models potentially represent the majority of the human population and enable evaluation of the safety and efficacy of novel and repurposed interventions against SARS-CoV-2 using endpoints of upper and lower respiratory tract virus replication, in addition to CT and histopathology in the assessment of significant but transient lung injury. However, further work is needed to develop models that are representative of the more severe outcomes that would particularly enable evaluation of the impact of therapies on host mediated pathology associated with high levels of prolonged, pulmonary disease. Given the limitations in reproducing the range of underlying health conditions in humans that link to poorer infection outcomes (e.g. diabetes, obesity and age) in macaques, other strategies of disease enhancement such as challenge, route, dose, strain, or manipulation of the host immunity, will be required.

The limited supply of rhesus macaques is now impacting on future COVID-19 studies to support the development of vaccines and therapeutic products [37]. The potential offered by cynomolgus macaques as an appropriate model will greatly increase the international community's ability to perform these critical studies in support of pre-clinical evaluation and product licensure. Moreover, cynomolgus macaques with a Mauritian genotype have more restricted genetic variability and more limited and better-defined MHC, providing an advantage in the battle to elucidate correlates of protective immunity. These features have been of particular value in HIV vaccine research where models are established in both rhesus macaques (Indian genotype) and cynomolgus macaques (Mauritian genotype) [38]. The MHC homogeneity associated with the Mauritian cynomolgus macaque has reduced the variability between animals after vaccination and has enhanced comparisons of vaccine regimens. In addition, the improved consistency in outcome facilitates the use of fewer animals to obtain statistically significant results than would be required if more genetically diverse species were to be used.

METHODS

Animals

Six cynomolgus macaques of Mauritian origin (*Macaca fascicularis)* and six rhesus macaques of Indian origin (*Macaca mulatta)* were used in this study. Study groups comprised three males and three females of each species and all were adults aged 2 to 4 years and weighing between 2.89 and 4.85kg at time of challenge. Before the start of the experiment, socially compatible animals were randomly assigned to challenge groups, to minimise bias.

Animals were housed in compatible social groups, in cages in accordance with the UK Home Office Code of Practice for the Housing and Care of Animals Bred, Supplied or Used for Scientific Procedures (2014) and National Committee for Refinement, Reduction and Replacement (NC3Rs) Guidelines on Primate Accommodation, Care and Use, August 2006 [39]. Prior to challenge animals were housed at Advisory Committee on Dangerous Pathogens (ACDP) level two in cages approximately 2.5M high by 4M long by 2M deep, constructed with high level observation balconies and with a floor of deep litter to allow foraging. Following challenge animals were transferred to ACDP Level three and housed in banks of cages of similar construction placed in directional airflow containment systems that allowed group housing and environmental control whilst providing a continuous, standardised inward flow of fully conditioned fresh air identical for all groups. Additional environmental enrichment was afforded by the provision of toys, swings, feeding puzzles and DVDs for visual stimulation. In addition to ad libitum access to water and standard old-world primate pellets, diet was supplemented with a selection of fresh vegetables and fruit. All experimental work was conducted under the authority of a UK Home Office approved project license (PDC57C033) that had been subject to local ethical review at PHE Porton Down by the Animal Welfare and Ethical Review Body (AWERB) and approved as required by the Home Office Animals (Scientific Procedures) Act 1986. Animals were sedated by intramuscular (IM) injection with ketamine hydrochloride (Ketaset, 100mg/ml, Fort Dodge Animal Health Ltd, Southampton, UK; 10mg/kg) for procedures requiring removal from their housing. None of the animals had been used previously for experimental procedures.

Viruses and Cells.

SARS-CoV-2 Victoria/01/2020[40] was generously provided by The Doherty Institute, Melbourne, Australia at P1 after primary growth in Vero/hSLAM cells and subsequently passaged twice at PHE Porton in Vero/hSLAM cells [ECACC 04091501]. Infection of cells was with ~0.0005 MOI of virus and harvested at day 4 by dissociation of the remaining attached cells by gentle rocking with sterile 5 mm borosilicate beads followed by clarification by centrifugation at 1,000 x g for 10 mins. Whole genome sequencing was performed, on the P3 challenge stock, using both Nanopore and Illumina as described previously[41]. Virus titre of the challenge stocks was determined by plaque assay on Vero/E6 cells [ECACC 85020206]. Cell lines were obtained from the European Collection of Authenticated Cell Cultures (ECACC) PHE, Porton Down, UK. Cell cultures were maintained at 37°C in Minimum essential medium (MEM) (Life Technologies, California, USA) supplemented with 10% foetal bovine serum (FBS) (Sigma, Dorset, UK) and 25 mM HEPES (Life Technologies, California, USA). In addition, Vero/hSLAM cultures were supplemented with 0.4

mg/ml of geneticin (Invitrogen) to maintain the expression plasmid. Challenge substance dilutions were conducted in phosphate buffer saline (PBS). Inoculum (5 x 10^6 PFU) was delivered by intratracheal route (2 ml) and intranasal instillation (1.0 ml total, 0.5 ml per nostril).

Clinical signs and in-life imaging by computerised tomography

Weight and body temperature were monitored daily. Nasal washes, throat and rectal swabs were taken at intervals of three days for each individual, having samples from at least two animals for each species until five dpc. Whole blood and serum were collected at the same time points. Nasal washes were obtained by flushing the nasal cavity with 2 ml PBS. For throat swabs, a flocked swab (MWE Medical Wire, Corsham, UK) was gently stroked across the back of the pharynx in the tonsillar area. Throat and rectal swabs were processed, and aliquots stored in viral transport media (VTM) and AVL buffer (Qiagen, Milton Keynes, UK) at -80^{o}C until assay.

Animals were monitored multiple times per day for behavioural and clinical changes. Behaviour was evaluated for contra-indicators including depression, withdrawal from the group, aggression, changes in feeding patterns, breathing pattern, respiration rate and cough. Prior to blood sample collection, aerosol challenge and euthanasia, animals were weighed, examined for gross abnormalities and body temperature measured.

CT scans were performed at 18 dpc from the four remaining animals at this time point. CT imaging was performed on sedated animals using a 16 slice Lightspeed CT scanner (General Electric Healthcare, Milwaukee, WI, USA) in the prone and supine position to assist the differentiation of pulmonary changes at the lung bases caused by gravity dependant atelectasis, from ground glass opacity caused by SARS-CoV-2. All axial scans were performed at 120 KVp, with Auto mA (ranging between 10 and 120) and were acquired using a small scan field of view. Rotation speed was 0.8 s. Images were displayed as an 11 cm field of view. To facilitate full examination of the cardiac and pulmonary vasculature, lymph nodes and extrapulmonary tissues, Niopam 300 (Bracco, Milan, Italy), a non-ionic, iodinated contrast medium, was administered intravenously (IV) at 2 ml/kg body weight and scans were collected immediately after injection and ninety seconds from the mid-point of injection. Scans were evaluated by an expert thoracic radiologist, blinded to the animal's clinical status, for the presence of: disease features characteristic of COVID-19 in humans (ground glass opacity (GGO), consolidation, crazy paving, nodules, peri-lobular consolidation; distribution: upper, middle, lower, central 2/3, bronchocentric); pulmonary embolus and the extent of any abnormalities estimated (<25%, 25-50%, 51-75%, 76-100%).

Post-mortem examination and histopathology

Animals were euthanised at 3 different time-points, in groups of four (including one animal from each species and sex) at 4/5, 14/15 and 18/19 dpc.

Animals were anaesthetised with ketamine (17.9 mg/kg bodyweight) and exsanguination was performed via cardiac puncture, followed by injection of an anaesthetic overdose (sodium pentabarbitone Dolelethal, Vetquinol UK Ltd, 140 mg/kg) to ensure euthanasia. Post-mortem examination and sample collection was performed immediately after confirmation of death.

The bronchial alveolar lavage fluid (BAL) was collected at necropsy from the right lung. The left lung was dissected prior to BAL collection and used for subsequent histopathology and virology procedures. At necropsy nasal washes, throat and rectal swabs, whole blood and serum were taken alongside tissue samples for histopathology.

Samples from the left cranial and left caudal lung lobe together with spleen, kidney, liver, mediastinal and axillary lymph nodes, small intestine (duodenum, jejunum and ileum), large intestine (caecum and colon), encephalon (cerebrum, cerebellum and brainstem), eye, trachea, larynx and nasal cavity, were fixed by immersion in 10% neutral-buffered formalin and processed routinely into paraffin wax. Nasal cavity samples were decalcified using an EDTA-based solution prior to embedding. Four µm sections were cut and stained with haematoxylin and eosin (H&E) and examined microscopically. A lung histopathology scoring system was setup and used to evaluate the severity of the histopathological lesions observed in each animal (Table 1), including lesions affecting the airways and the parenchyma. Three tissue sections from each left lung lobe were used to evaluate the lung histopathology.

In addition, samples were stained using the RNAscope technique to identify the SARS-CoV-2 virus RNA or Interleukin 6 (IL-6) in lung tissue sections. Briefly, tissues were pre-treated with hydrogen peroxide for 10 mins (RT), target retrieval for 15 mins (98-102°C) and protease plus for 30 mins (40°C) (Advanced Cell Diagnostics). A V-nCoV2019-S probe (SARS-CoV-2 Spike gene specific), or host species specific IL-6-S probes (Advanced Cell Diagnostics, Bio-techne) were incubated on the tissues for two hours at 40°C. In addition, samples were stained using the RNAscope technique to identify the SARS-CoV-2 virus RNA. Amplification of the signal was carried out following the RNAscope protocol using the RNAscope 2.5 HD Detection kit – Red (Advanced Cell Diagnostics, Biotechne).

Digital image analysis was performed in RNAscope labelled slides to ascertain the percentage of stained cells within the lesions, by using the Nikon-NIS-Ar package. The presence of viral RNA by ISH was evaluated using the whole lung tissue section slides. For IL-6 mRNA, the areas of histopathological lesions were selected as regions of interest (ROI) and the positively labelled area (red) was calculated by the software after setting the thresholds.

Viral load quantification by RT-qPCR

RNA was extracted using the QIAamp Viral RNA Mini Kit (Qiagen) following manufacturer's instruction with final elution in 60 µl nuclease free water. Reverse transcription-quantitative polymerase chain reaction (RT-qPCR) was performed using TaqPath™ 1-Step RT-qPCR Master Mix, CG (Applied Biosystems™), 2019-nCoV CDC RUO Kit (Integrated DNA Technologies) and 7500 Fast Real-Time PCR System (Applied Biosystems™) as previously described [42]. PCR amplicons were quantified against 2019-nCoV_N_Positive Control (Integrated DNA Technologies). Positive samples detected below the lower limit of quantification (LLOQ) of 20 copies/µl were assigned the value of 13 copies/µl, undetected samples were assigned the value of ≤6.2 copies/µl, equivalent to the assays LLOD. For extracted samples this equates to an LLOQ of 8.57×10^3 copies/ml and LLOD of 2.66×10^3 copies/ml.

Plaque assay

Samples were incubated in 24-well plates (Nunc, ThermoFisher Scientific, Loughborough, UK) containing twice washed with Dulbecco's PBS (DPBS) monolayers of Vero E6 cells seeded the previous day at 1.5 x 10^5 cells/well under Overlay media consisting of MEM (Life Technologies) containing 1.5% carboxymethylcellulose (Sigma), 4% (v/v) heat-inactivated foetal calf serum (FCS) (Sigma) and 25mM HEPES buffer (Gibco). After incubation at 37ºC for 120 hours, they were fixed overnight with 10% (w/v) formalin/PBS, washed with tap water and stained with methyl crystal violet solution (0.2% v/v in 40% (v/v) Ethanol) (Sigma).

Plaque reduction neutralisation test

Neutralising virus titres were measured in heat-inactivated (56°C for 30 minutes) serum samples. SARS-CoV-2 was diluted to a concentration of 1.4 x 10^3 pfu/ml (70 pfu/50 µl) and mixed 50:50 in 1% FCS/MEM with doubling serum dilutions from 1:10 to 1:320 in a 96-well V-bottomed plate. The plate was incubated at 37°C in a humidified box for one hour to allow the antibody in the serum samples to neutralise the virus. The neutralised virus was transferred into the wells of a washed plaque assay 24-well plate (see plaque assay method), allowed to adsorb at 37°C for a further hour, and overlaid with plaque assay overlay media. After five days incubation at 37°C in a humified box, the plates were fixed, stained and plaques counted.

A mid-point probit analysis was used to determine the dilution of antibody required to reduce SARS-CoV-2 viral plaques by 50% (PRNT50) compared with the virus only control (n=5). Analysis was conducted in R [43] and the script was based on a source script from Johnson et al., 2013 [44].

ELISA

A full length trimeric and stabilised version of the SARS-CoV-2 Spike protein (amino acids 1-1280, GenBank: MN MN908947) was developed and kindly provided by Florian Krammer's lab as previously described [45]. Recombinant SARS-CoV-2 Receptor-Binding-Domain (319-541) Myc-His was developed and kindly provided by MassBiologics, USA. Recombinant SARS-CoV-2 Nucleocapsid phosphoprotein (GenBank: MN908947, isolate Wuhan-Hu-1) was expressed and purified from Escherichia coli as full-length nucleoprotein (amino acids 1-419) with a C-terminal 6xHis-Tag (REC31812-100, Batch #20042310, Native Antigen Company).

Spike-, Spike RBD- and NP-specific IgG responses were determined by ELISA. High-binding 96-well plates (Nunc Maxisorp) were coated with 50 µl per well of 2 µg/ml Spike trimer, Spike RBD or NP in 1X PBS (Gibco) and incubated overnight at 4°C. The ELISA plates were washed five times with wash buffer (1 X PBS/0.05% Tween 20 (Sigma)) and blocked with 100 µl/well 5% FBS (Sigma)) in 1 X PBS/0.1% Tween 20 for one hour at room temperature. After washing, serum samples previously 0.5% Triton-inactivated were serially diluted in 10% FBS in 1 X PBS/0.1% Tween 20, 50 µl/well of each dilution were added to the antigen coated plate and incubated for two hours at room temperature. Following washing, anti-monkey IgG conjugated to HRP (Invitrogen) were diluted (1:10,000) in 10% FBS in 1 X PBS/0.1%

Tween 20 and 100 µl/well were added to the plate, then incubated for one hour at room temperature. After washing, 1 mg/ml O-Phenylenediamine dihydrochloride solution (Sigma) was prepared and 100 µl per well were added. The development was stopped with 50 µl per well 1 M Hydrochloric acid (Fisher Chemical, J/4320/15) and the absorbance at 490 nm was read using Softmax 7.0. Endpoint titres and statistical analyses (Kruskal-Wallis one-way ANOVA) were performed with Graph Pad Prism 8.0. The cut-off was set at the average Optical Density of samples collected from naïve animals (Day 0) + 3 Standard Deviation.

Mononuclear cell Isolation

PBMCs were isolated from whole blood anticoagulated with heparin (132 Units per 8 ml blood) (BD Biosciences, Oxford, UK) using standard methods. Of note is that the material used for density gradient centrifugation was adjusted dependent on the macaque species, with a Ficoll Histopaque gradient (GE Healthcare, USA) used with Rhesus macaque blood and a Percoll gradient (GE Healthcare) used with cynomolgus macaques. Mononuclear cells (MNC) were isolated from spleen and lung tissue samples using an OctoMACS tissue dissociation device (Miltenyi Biotec). Lung tissue samples were dissected into approximately 5mm^3 pieces and incubated for one hour in a solution of 772.8 U/ml collagenase + 426 U/ml DNase (both from Sigma) diluted in Earle's balanced salt solution supplemented with 200 mg/ml Calcium Chloride (Gibco, Life Technologies, Renfrew, UK), at 37ºC with continual gentle mixing of the tube. The homogenised solution was passed through a 70 µm cell filter (BD Biosciences) and the mononuclear cells separated by Ficoll Histopaque density gradient centrifugation. PBMCs and MNC isolated from tissues were stored at −180 °C until resuscitated for analysis.

Resuscitation of cryopreserved cells

PBMCs and MNC were thawed, washed in R10 medium (consisting of RPMI 1640 supplemented with 2 mM L-glutamine, 50 U/ml penicillin- 50 µg/ml streptomycin, and 10% heat-inactivated FBS) with 1 U/ml of DNase (Sigma), and resuspended in R10 medium and incubated at 37°C 5% CO_2 overnight.

ELISPOT

An IFNγ ELISpot assay was used to estimate the frequency and IFNγ production capacity of SARS-CoV-2-specific T cells in PBMCs using a human / simian IFNγ kit (MabTech, Nacka. Sweden), as described previously [46]. The cells were assayed at 2 x 10^5 cells per well, unless there were not enough cells, in which case 1 x 10^5 cells were used. Cells were stimulated overnight with SARS-CoV-2 peptide pools and ‘megapools’ of the spike protein (Mimotopes, Australia). Ten peptide pools were used, comprising of 15mer peptides, overlapping by 11 amino acids. The three megapools were made up as such: Megapool 1 (MP1) comprised peptide pools 1-3, Megapool 2 (MP2) comprised peptide pools 4-6 and Megapool 3 (MP3) comprised of peptide pools 7-10. All peptides were used at a concentration of 1.7 µg per well. Phorbol 12-myristate (Sigma) (100 ng/ml) and ionomycin (CN Biosciences, Nottingham, UK) (1 mg/ml) were used as a positive control. Results were calculated to report as spot forming units (SFU) per million cells. All SARS-CoV-2 peptides and megapools were assayed in duplicate and media only wells subtracted to give the antigen-specific SFU. ELISPOT plates were analysed using the CTL scanner and software (CTL, Germany) and further analysis carried out using GraphPad Prism (version 8.0.1) (GraphPad Software, USA) Immunophenotyping and Intracellular cytokine staining assays. Naïve animal samples were taken from previous studies.

Intracellular cytokine staining (ICS) and immunophenotyping assays were performed using 1 x 10^6 PBMC or MNC in R10 medium (described above). For intracellular cytokine staining, these cells were stimulated with a 10 μg/ml solution of CD28 and CD49d co-stimulatory antibodies (both from BD Biosciences) and 1ug/ml of 15-mer overlapping peptide pools spanning either the SARS-CoV-2 spike (S), nucleocapsid (N) or membrane glycoprotein (M) sequence (Miltenyi Biotec, Bisley, UK) or 5 μg/ml staphylococcal enterotoxin b (SEB) (Sigma), or R10 medium with matched concentration of DMSO as negative control, for a total of 16 hours at 37°C, in a 5% CO_2 supplemented incubator. Anti-CD107a-AF488 (BD Biosciences) was included during cell stimulations. Following the initial two hours of incubation, the protein transport inhibitor Brefeldin-A (Sigma) was added at a final concentration of 10 μg/ml. Following incubation, cells were washed with FACS buffer consisting of PBS + 1% FCS and incubated for 30 minutes at room temperature with optimal dilutions of the amine-reactive Live/Dead Fixable Red viability cell stain (Life Technologies) and the antibodies CD4 PerCP-Cy5.5, CD8 APC-Fire750, CD69-BV510, (all from BD Biosciences) and CD20- Pe-Dazzle-594, γδ-TCR-BV421 (Biolegend, London, UK) prepared in BD Biosciences Brilliant stain buffer (BD Biosciences, Oxford, UK). Following surface marker staining, the cells were washed and then permeabilised by incubation at room temperature for 15 minutes with Fix/Perm reagent (BD Biosciences) before washing with Permwash buffer (BD Biosciences). Intracellular antigen staining was applied by incubation at room temperature for 30 minutes with the antibodies CD3-AF700, IFN-γ-PeCy7, TNF-α-BUV395, GM-SCF-PE (all from BD

Biosciences, Oxford, United Kingdom), IL-2-APC (Miltenyi Biotech Ltd), IL-17-BV711 (Biolegend, London, UK) prepared in brilliant stain buffer. For immunophenotyping assays, cells were washed with FACs buffer by centrifugation before staining with amine-reactive Live/Dead Fixable violet viability cell stain as per the manufacturer's instructions (Life Technologies). Cells were then incubated for 30 minutes at room temperature with optimal dilutions of the following antibodies: anti-CD4-PerCP-Cy5.5, anti-CD8-APC-Fire750 anti-CD11c-PE. anti-CD14-APC, anti-CD16-BV786, anti-CD20-PE-Dazzle (all from BioLegend); anti-CD3-AF700, anti-CD56-BV605, anti-HLA-DR-BUV395 (all from BD Biosciences); anti-CD159a-PC7 (Beckman Coulter) prepared in brilliant stain buffer. BD Compbeads (BD Biosciences) were labelled with the above fluorochromes for use as compensation controls. Following antibody labelling, cells and beads were washed by centrifugation and fixed in 4% paraformaldehyde solution (Sigma) prior to flow cytometric acquisition.

Flow cytometric acquisition and analysis.

Cells were analysed using a five laser LSRII Fortessa instrument (BD Biosciences) and data were analysed using FlowJo (version 9.7.6, BD Biosciences). Cytokine-producing T-cells were identified using a forward scatter-height (FSC-H) versus side scatter-area (SSC-A) dot plot to identify the lymphocyte population, to which appropriate gating strategies were applied to exclude doublet events, non-viable cells and B cells (CD20$^+$). For ICS analysis, sequential gating through CD3$^+$, followed by CD4$^+$ or CD8$^+$ gates were used before individual cytokine gates to identify IFN-γ, IL-2, TNF-α, GM-CSF and IL-17, CD107a and CD69 stained populations. In immunophenotyping data sets, classical-, non-classical-monocytes and monocyte derived dendritic cells (mDCs) were identified by FSC and SSC characteristics and by the expression pattern of HLA-DR, CD14, CD16 and CD11c within the live CD3$^-$, CD20$^-$ population. Similarly, natural killer cells subsets were identified by expression of CD8, CD159a, CD56 and CD16 within live CD3$^-$ lymphocyte subsets. Polyfunctional cells were identified using Boolean gating combinations of individual cytokine-producing CD4 or CD8 T-cells. The software package PESTLE version 1.7 (Mario Roederer, Vaccine Research Centre, NIAID, NIH) was used for background subtraction to obtain antigen-specific polyfunctional ICS cytokine responses, Graphpad Prism (version 8.0.1) was used to generate graphical representations of flow cytometry data.

DATA AVAILABILITY:

All data and materials used in the analysis are presented in the main text and supplementary figures

REFERENCES:

1 Falsey, A. R. & Walsh, E. E. Novel coronavirus and severe acute respiratory syndrome. *Lancet* **361**, 1312-1313, doi:10.1016/S0140-6736(03)13084-X (2003).

2 de Groot, R. J. *et al.* Middle East respiratory syndrome coronavirus (MERS-CoV): announcement of the Coronavirus Study Group. *J Virol* **87**, 7790-7792, doi:10.1128/JVI.01244-13 (2013).

3 Callaway, E., Cyranoski, D., Mallapaty, S., Stoye, E. & Tollefson, J. The coronavirus pandemic in five powerful charts. *Nature* **579**, 482-483, doi:10.1038/d41586-020-00758-2 (2020).

4 WHO. WHO SITREP 164

5 Chen, N. *et al.* Epidemiological and clinical characteristics of 99 cases of 2019 novel coronavirus pneumonia in Wuhan, China: a descriptive study. *Lancet* **395**, 507-513, doi:10.1016/S0140-6736(20)30211-7 (2020).

6 Huang, C. *et al.* Clinical features of patients infected with 2019 novel coronavirus in Wuhan, China. *Lancet* **395**, 497-506, doi:10.1016/S0140-6736(20)30183-5 (2020).

7 Subbarao, K. & Roberts, A. Is there an ideal animal model for SARS? *Trends Microbiol* **14**, 299-303, doi:10.1016/j.tim.2006.05.007 (2006).

8 Roberts, A. *et al.* Animal models and vaccines for SARS-CoV infection. *Virus Res* **133**, 20-32, doi:10.1016/j.virusres.2007.03.025 (2008).

9 McAuliffe, J. *et al.* Replication of SARS coronavirus administered into the respiratory tract of African Green, rhesus and cynomolgus monkeys. *Virology* **330**, 8-15, doi:10.1016/j.virol.2004.09.030 (2004).

10 Rowe, T. *et al.* Macaque model for severe acute respiratory syndrome. *J Virol* **78**, 11401-11404, doi:10.1128/JVI.78.20.11401-11404.2004 (2004).

11 Chandrashekar, A. *et al.* SARS-CoV-2 infection protects against rechallenge in rhesus macaques. *Science*, doi:10.1126/science.abc4776 (2020).

12 Munster, V. J. *et al.* Respiratory disease in rhesus macaques inoculated with SARS-CoV-2. *Nature*, doi:10.1038/s41586-020-2324-7 (2020).

13 Rockx, B. *et al.* Comparative pathogenesis of COVID-19, MERS, and SARS in a nonhuman primate model. *Science*, doi:10.1126/science.abb7314 (2020).

14 Caly, L. *et al.* Isolation and rapid sharing of the 2019 novel coronavirus (SARS-CoV-2) from the first patient diagnosed with COVID-19 in Australia. *Med J Aust* **212**, 459-462, doi:10.5694/mja2.50569 (2020).

15 Yu, J. *et al.* DNA vaccine protection against SARS-CoV-2 in rhesus macaques. *Science*, doi:10.1126/science.abc6284 (2020).

16 van Doremalen, N. *et al.* A single dose of ChAdOx1 MERS provides protective immunity in rhesus macaques. *Sci Adv* **6**, eaba8399, doi:10.1126/sciadv.aba8399 (2020).

17 Maisonnaise P, G. J., Contresras V, Behillil S, Solas C, Marlin R, Naninck T, Izzorno A, Lemaitre Jet al. . Hydroxychloroquine in the treatment and prophylaxis of SARS-CoV-2 infection in non- human primates. (2020).

18 Yang, X. *et al.* Clinical course and outcomes of critically ill patients with SARS-CoV-2 pneumonia in Wuhan, China: a single-centered, retrospective, observational study. *Lancet Respir Med* **8**, 475-481, doi:10.1016/S2213-2600(20)30079-5 (2020).

19 Arentz, M. *et al.* Characteristics and Outcomes of 21 Critically Ill Patients With COVID-19 in Washington State. *JAMA*, doi:10.1001/jama.2020.4326 (2020).

20 Guan, W. J. *et al.* Clinical Characteristics of Coronavirus Disease 2019 in China. *N Engl J Med* **382**, 1708-1720, doi:10.1056/NEJMoa2002032 (2020).

21 Singh, D. K. *et al.* SARS-CoV-2 infection leads to acute infection with dynamic cellular and inflammatory flux in the lung that varies across nonhuman primate species. 2020.2006.2005.136481, doi:10.1101/2020.06.05.136481 %J bioRxiv (2020).

22 van Doremalen, N. *et al.* ChAdOx1 nCoV-19 vaccination prevents SARS-CoV-2 pneumonia in rhesus macaques. 2020.2005.2013.093195, doi:10.1101/2020.05.13.093195 %J bioRxiv (2020).

23 Carsana, L. *et al.* Pulmonary post-mortem findings in a series of COVID-19 cases from northern Italy: a two-centre descriptive study. *Lancet Infect Dis*, doi:10.1016/S1473-3099(20)30434-5 (2020).

24 Herold, T. *et al.* Elevated levels of IL-6 and CRP predict the need for mechanical ventilation in COVID-19. *J Allergy Clin Immunol*, doi:10.1016/j.jaci.2020.05.008 (2020).

25 Chen, X. *et al.* Detectable serum SARS-CoV-2 viral load (RNAaemia) is closely correlated with drastically elevated interleukin 6 (IL-6) level in critically ill COVID-19 patients. *Clin Infect Dis*, doi:10.1093/cid/ciaa449 (2020).

26 Vabret, N. *et al.* Immunology of COVID-19: Current State of the Science. *Immunity* **52**, 910-941, doi:10.1016/j.immuni.2020.05.002 (2020).

27 Huang, A. T. *et al.* A systematic review of antibody mediated immunity to coronaviruses: antibody kinetics, correlates of protection, and association of antibody responses with severity of disease. *medRxiv*, doi:10.1101/2020.04.14.20065771 (2020).

28 Giamarellos-Bourboulis, E. J. *et al.* Complex Immune Dysregulation in COVID-19 Patients with Severe Respiratory Failure. *Cell Host Microbe* **27**, 992-1000 e1003, doi:10.1016/j.chom.2020.04.009 (2020).

29 Diao, B. *et al.* Reduction and Functional Exhaustion of T Cells in Patients With Coronavirus Disease 2019 (COVID-19). *Front Immunol* **11**, 827, doi:10.3389/fimmu.2020.00827 (2020).

30 Zheng, M. *et al.* Functional exhaustion of antiviral lymphocytes in COVID-19 patients. *Cell Mol Immunol* **17**, 533-535, doi:10.1038/s41423-020-0402-2 (2020).

31 Yonggang Zhou, B. F., Xiaohu Zheng, Dongsheng Wang, Changcheng Zhao, Yingjie Qi, Rui Sun, Zhigang Tian, Xiaoling Xu, Haiming Wei Pathogenic T-cells and inflammatory monocytes incite inflammatory storms in severe COVID-19 patients. *National Science Review* **7**, 5 (2020).

32 Grifoni, A. *et al.* Targets of T Cell Responses to SARS-CoV-2 Coronavirus in Humans with COVID-19 Disease and Unexposed Individuals. *Cell* **181**, 1489-1501 e1415, doi:10.1016/j.cell.2020.05.015 (2020).

33 Zhao, J. *et al.* Airway Memory CD4(+) T Cells Mediate Protective Immunity against Emerging Respiratory Coronaviruses. *Immunity* **44**, 1379-1391, doi:10.1016/j.immuni.2016.05.006 (2016).

34 Juno, J. A. *et al.* Humoral and circulating follicular helper T cell responses in recovered patients with COVID-19. *Nat Med*, doi:10.1038/s41591-020-0995-0 (2020).

35 Thanh Le, T. *et al.* The COVID-19 vaccine development landscape. *Nat Rev Drug Discov* **19**, 305-306, doi:10.1038/d41573-020-00073-5 (2020).

36 Skinner, J. M. *et al.* Comparison of rhesus and cynomolgus macaques in a Streptococcus pyogenes infection model for vaccine evaluation. *Microb Pathog* **50**, 39-47, doi:10.1016/j.micpath.2010.10.004 (2011).

37 Zhang, S. America Is Running Low on a Crucial Resource for COVID-19 Vaccines. *The Atlantic* (2020).

38 Sui, Y., Gordon, S., Franchini, G. & Berzofsky, J. A. Nonhuman primate models for HIV/AIDS vaccine development. *Curr Protoc Immunol* **102**, Unit 12 14, doi:10.1002/0471142735.im1214s102 (2013).

39 National Committee for Refinement, R. a. R. N. R. G. o. P. A., Care and Use. Non human primate accomodation, care and use. (2006).

40 Caly, L. *et al.* Isolation and rapid sharing of the 2019 novel coronavirus (SARS-CoV-2) from the first patient diagnosed with COVID-19 in Australia. **n/a**, doi:10.5694/mja2.50569.

41 Lewandowski, K. *et al.* Metagenomic Nanopore Sequencing of Influenza Virus Direct from Clinical Respiratory Samples. *Journal of Clinical Microbiology* **58**, e00963-00919, doi:10.1128/JCM.00963-19 (2019).

42 Ryan, K. A. *et al.* Dose-dependent response to infection with SARS-CoV-2 in the ferret model: evidence of protection to re-challenge. 2020.2005.2029.123810, doi:10.1101/2020.05.29.123810 %J bioRxiv (2020).

43 Team, R. C. R: A language and environment for statistical computing. *R Foundation for Statistical Computing, Vienna, Austria* (2019).

44 Johnson, R. M., Dahlgren, L., Siegfried, B. D. & Ellis, M. D. Acaricide, fungicide and drug interactions in honey bees (Apis mellifera). *PLoS One* **8**, e54092, doi:10.1371/journal.pone.0054092 (2013).

45 Amanat, F. *et al.* A serological assay to detect SARS-CoV-2 seroconversion in humans. *Nat Med*, doi:10.1038/s41591-020-0913-5 (2020).

46 Sibley, L. S. *et al.* ELISPOT Refinement Using Spot Morphology for Assessing Host Responses to Tuberculosis. *Cells* **1**, 5-14, doi:10.3390/cells1010005 (2012).

Acknowledgments: The authors would like to thank J. Druce and M.G. Catton from the Victorian Infectious Diseases Reference Laboratory, Royal Melbourne Hospital, At the Peter Doherty Institute for Infection and Immunity, Victoria, 3000, Australia, for providing the SARS-CoV-2 isolate used in this study. This work was funded by the Coalition of Epidemic Preparedness Innovations (CEPI).

Author contributions: FJS, KAR, YH, JAT, SGF, KRBw, SS, MJD, SC, BH, and MWC conceived the study. FJS, LH, CLK, GP, ELR and AGN performed the pathological analyses. ADW, LS, CS, SLo, O D-P, KG, AM, ALM and TT performed the immunological studies. KRBw grew viral stock and optimised virology techniques. SAF, PB, BEC, RC, DJH, TH, CMKH, VL, DN, JP, IT, ST, NRW and MJD performed animal procedures and sampling processing. GSS, KEG, HEH, RJW, LA, EB, KRBu, MA, NSC, DK, KJG, JG, RH, SLe, EJP, SP, CT and NW performed virological and molecular biology techniques. MJE performed statistical analyses. FVG devised the scan protocols, the scoring system and reported the CTscans. FJS, ADW, MJD, SS and MWC wrote the first draft of the manuscript that was accepted by all authors before submission.

Competing interests: No conflicts of interest declared.

FIGURE LEGENDS

Figure 1. Images constructed from CT scans collected 18 days after challenge with SARS-CoV-2 showing pulmonary abnormalities in two cynomolgus (A, B) and one rhesus macaque (C). Arrows indicate areas of ground glass opacification and consolidation.

Figure 2. Viral RNA detected by RT-qPCR. Viral load presented as the geometric mean of cDNA copies/ml, with individual data points overlaid in rhesus macaques (blue) and cynomolgus macaques (red) in A) nasal wash, B) throat swab, C) bronchoalveolar lavage (BAL) collected at necropsy (numbers indicate days post challenge the NHP was euthanised), D) rectal swab, and E) whole blood. Dashed lines highlight the LLOQ (lower limit of quantification, 8.57 x 10^3 copies/ml) and LLOD (lower limit of detection, 2.66 x10^3 copies/ml). Positive samples detected below the LLOQ were assigned the value of 5.57 x 10^3 copies/ml. Viral RNA was not detected in naïve animals (data not shown).

Figure 3. Histopathological changes in cynomolgus and rhesus macaques during SARS-CoV-2 infection. Diffuse areas of DAD observed in cynomolgus macaques at 4/5 dpc with shrunken, eosinophilic cells within the alveolar walls (A, B), together with alveolar oedema (A, arrows) pneumocyte hyperplasia and expanded alveolar spaces with inflammatory cell infiltration (B, arrows). Occasional multinucleated cells resembling syncytial cells are observed (B, insert). ISH detection of viral RNA (RNAScope, red chromogen) within the areas of pneumonia (C) and occasionally in the BALT (C, insert). Abundant IL-6 producing cells observed in the

areas of pneumonia (D) Similar histopathological changes observed in rhesus macaques, including DAD areas with patchy alveolar oedema (E, arrow), alveolar macrophage hyperplasia (F, arrow), bronchial exudates and presence of viral RNA within the areas showing pneumonia (G) and abundant IL-6 producing cells (H). Histopathological changes with less severity observed at 14/15 dpc in cynomolgus macaques, with infiltration of mononuclear cells within alveolar spaces and bronchiolar luminae (I, arrows) and parenchymal collapse (I, *) and perivascular cuffing (J, arrow), with minimal detection of viral RNA in pneumocytes (J, insert). Bronchiole regeneration (K, arrow) and perivascular/peribronchiolar cuffing observed in rhesus macaques at 14/15 dpc (L, arrows), together with BALT proliferation (L, *) with minimal presence of viral RNA (L, insert).

Figure 4. Lung histopathology scores and presence of viral RNA and IL-6 by ISH in cynomolgus and rhesus macaques during SARS-CoV-2 infection. Heatmap showing the individual and aggregate (TOTAL) scores for each lung histopathological parameter and animal (A). Image analysis of positively stained area in RNAScope labelled sections for viral RNA (B; whole slide) and IL-6 mRNA (C, areas of lesion), showing data for individual animals with mean value for each group (box).

Figure 5. Neutralizing antibodies in serum measured by Plaque reduction neutralisation test ($PRNT_{50}$). Serum neutralisation titres as reciprocal highest dilution resulting in an infection reduction of >50% in samples ($PRNT_{50}$) pre-challenge and at 1-3, 4-6, 8-9, 11-12 and 14-19 days post challenge in rhesus macaques (blue) and cynomolgus macaques (red). Bars indicating group mean +/- standard error with $PRNT_{50}$ determined for individual animals shown as circles and

squares respectively. Neutralizing antibodies were observed at 8-9 dpc at low levels, increasing from 11dpc onwards, with higher values in cynomolgus macaques compared to rhesus.

Figure 6. SARS-CoV-2-specific IgG antibodies measured by ELISA in naïve and SARS-CoV-2 infected macaques. Spike- (A), Receptor-Binding Domain- (B) and Nucleoprotein- (C) specific IgG antibodies measured in sera of rhesus and cynomolgus macaques. Sera were collected from uninfected animals (day 0) or 1-3, 4-6, 8-9, 11-12 and 14-19 days following SARS-CoV-2 infection. Bars show the group mean +/- SEM with an endpoint titre determined for each individual animal shown as squares for males and dots for females. * *$p \leq 0.05$ (Kruskal-Wallis one-way ANOVA).* Experiment performed in duplicates.

Figure 7. Cellular immune responses to SARS-CoV-2. A, B) IFNγ SFU measured in PBMCs and stimulated with spike protein peptide pools (PP) peptide in A) rhesus and B) cynomolgus macaques. PBMC samples were isolated from uninfected animals (naïve) or at early (days 4 and 5) and late (days 14-19) time-points following SARS-CoV-2 infection. Box plots show the group median +/- inter-quartile range, with minimum and maximum values connected by whiskers. C, D) IFNγ SFU measured in PBMC in response to spike protein megapools (MP) in C) rhesus and D) cynomolgus macaques or, E) in mononuclear cells isolated from lung and spleen. Bars show the group median with SFU measured in individual animals shown as dots. * $p \leq 0.05$, ** $p \leq 0.01$. F-J) Frequency of major lymphocyte and monocyte cell populations quantified by immunophenotyping assay F - H) CD4+, CD8+ and γδ T-cell frequencies in PBMCs and lung cells, I) Monocyte subtype frequency in PBMCs

and lung MNCs, J) Natural killer (NK) cell subset frequency in PBMCs and lung MNCs. Stacked bars show the group median with 95% confidence intervals. PBMC: Naïve rhesus n=8, early rhesus n= 1, late rhesus n=2, naïve cyno = 7, early cyno n=2, late cyno n=2. Lung: early rhesus n= 2, late rhesus n=3, early cyno n=2, late cyno n=2. K-N) Intracellular cytokine staining data K-L) Cytokine and activation marker detection in CD4+, CD8+ and γδ T-cells in PBMCs stimulated with M, N and S peptide pools. G-N) CD107a expression in CD8+ and γδ T-cells in PBMCs. Bars show the group median with cell frequencies measured in individual animals shown as dots.

Table 1. Pulmonary histopathology scoring system

Lesion	Score 0 (normal)	Score 1 (minimal)	Score 2 (mild)	Score 3 (moderate)	Score 4 (severe)
Bronchial **epithelial degeneration/necrosis with presence of exudates and/or inflammatory cell infiltration**	None	Occasional (1 or 2) bronchi affected.	Present in multiple airways; **up to 25% of bronchi affected**	Present in multiple airways; **between 26-50% of bronchi affected**	Present in multiple airways; **over 50% of bronchi affected**
Bronchiolar **(primarily terminal) epithelial degeneration/necrosis with presence of exudates and/or inflammatory cell infiltration**	None	Occasional (1 or 2) bronchioli affected	Present in multiple airways; **up to 25% of bronchioli affected**	Present in multiple airways; **between 26-50% of bronchioli affected**	Present in multiple airways; **over 50% of bronchioli affected**
Perivascular **inflammatory infiltrates (cuffing)**	None	**Occasional** incomplete, or loosely formed cuffs	**Numerous** cuffs; predominantly **incomplete** and **loosely formed** with **lesser well-formed complete cuffs**	**Numerous** cuffs; approximately **half or more** well-formed, and may have **few broad, dense cuffs**	**Numerous** cuffs; **predominantly well-formed** with **numerous broad, dense cuffs**
Peribronchiolar **inflammatory infiltrates (cuffing)**	None	**Occasional** incomplete, or loosely formed cuffs	**Numerous** cuffs; predominantly **incomplete** and **loosely formed** with **lesser well-formed complete cuffs**	**Numerous** cuffs; approximately **half or more** well-formed, and may have **few broad, dense cuffs**	**Numerous** cuffs; **predominantly well-formed** with **numerous broad, dense cuffs**
Acute diffuse alveolar damage (necrosis of pneumocytes)	None	Small numbers of foci; **up to 5% of slide affected**	Multiple foci; **between 6-25% of the slide affected**	Increased numbers of foci; between **26-50% of the slide affected**	Numerous foci; over **50% of the slide affected**
Alveolar cellular exudate and oedema and/or fibrin	None (alveolar macrophages at physiological levels)	**Occasional** alveoli; **up to 5% of slide affected**	Confluent alveoli; between **6-25% of the slide affected**	Confluent alveoli; between **26-50% of the slide affected**	Confluent alveoli; **affecting over 50% of the slide**
Alveolar septal inflammatory cells and cellularity	Normal septae; typically 1-2 (occasionally 3) nucleated cells wide; absence of inflammatory cells	Thickening of the alveolar walls by inflammatory cells; **up to 5% of the slide affected**	Thickening of the alveolar walls by inflammatory cells; **between 6-25% of the slide affected**	Thickening of the alveolar walls by inflammatory cells; **between 26-50% of the slide affected**	Thickening of the alveolar walls by inflammatory cells; **over 50% of the slide affected**

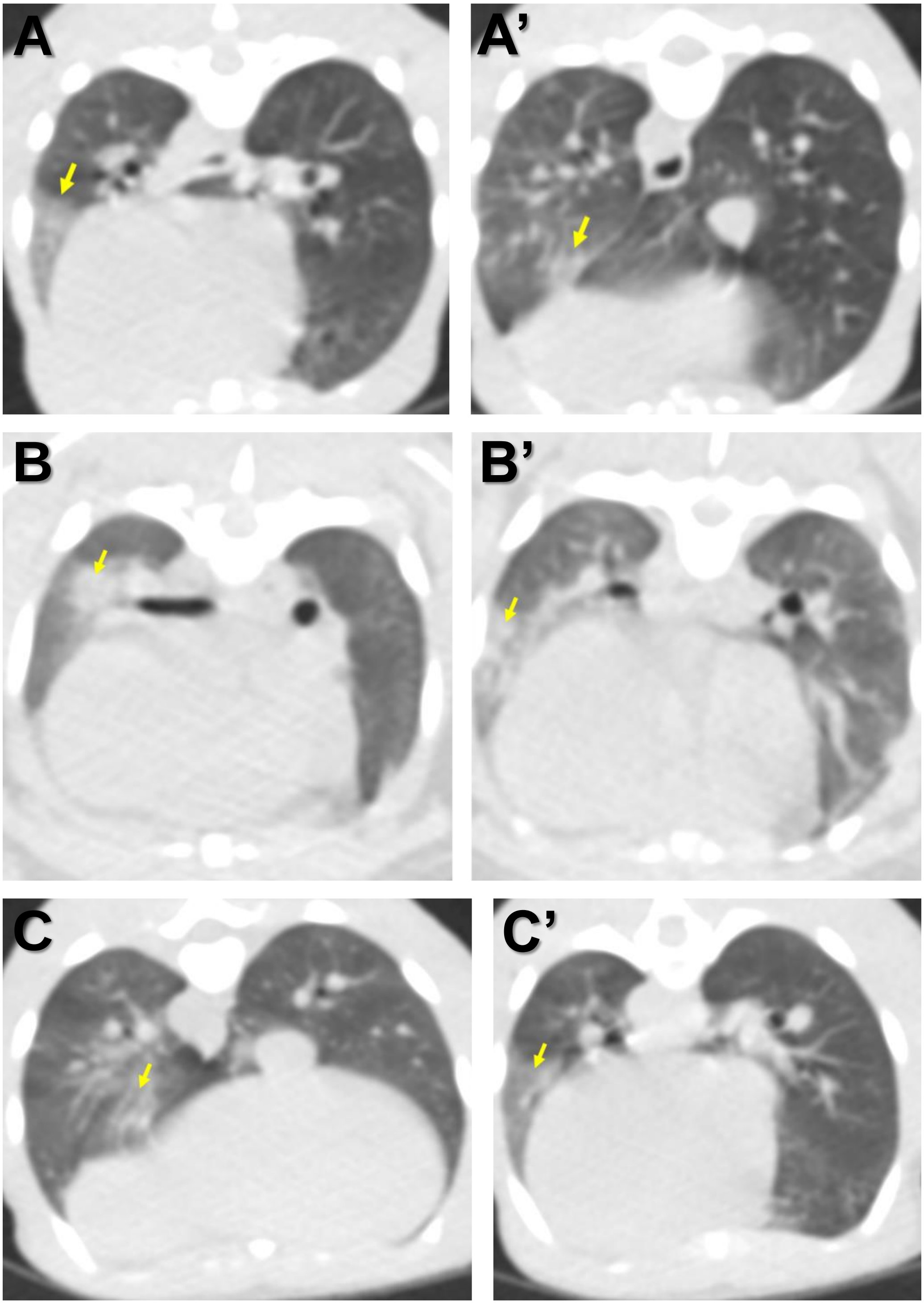
A
A’
B
B’
C
C’

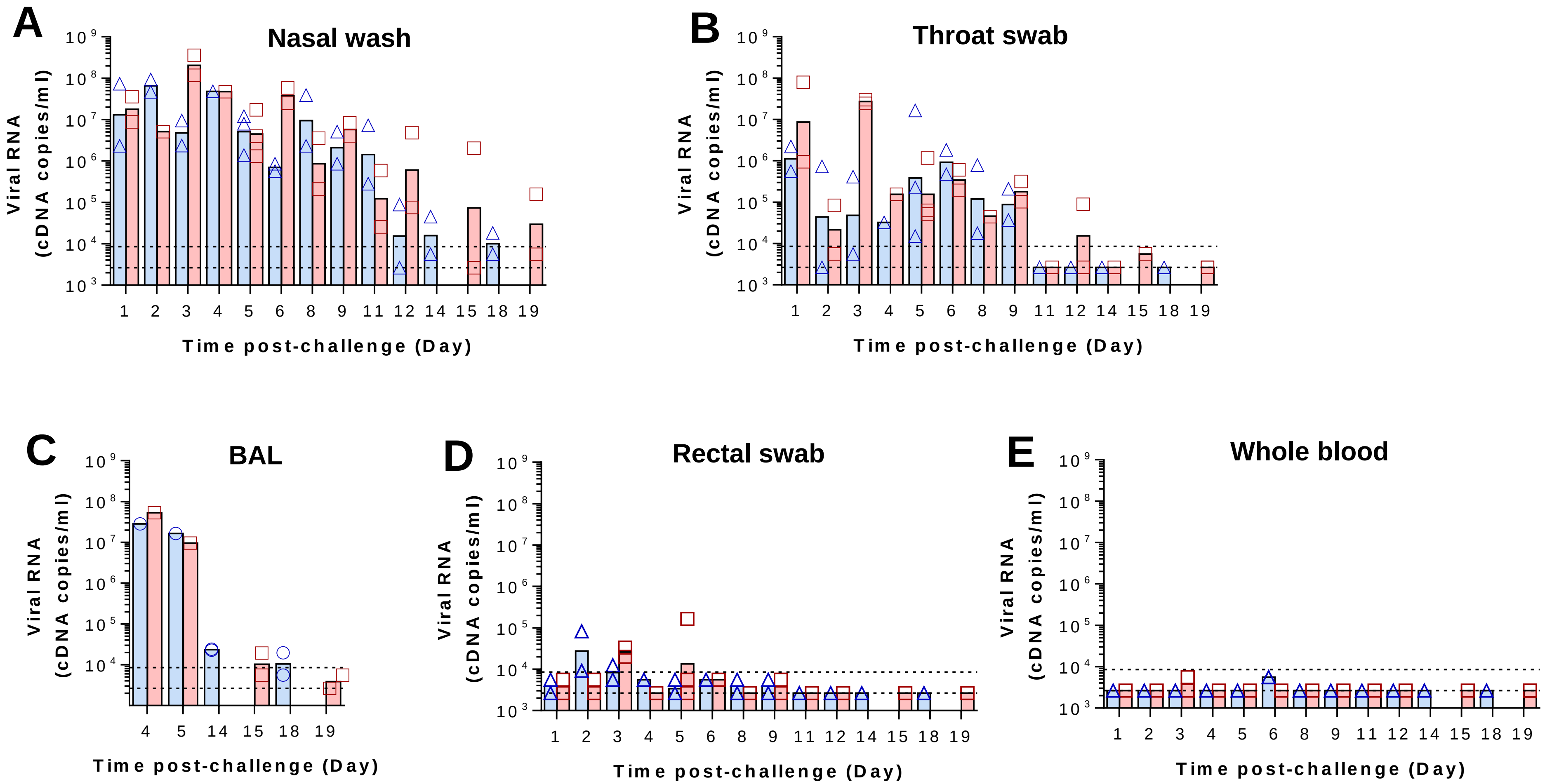
A
Nasal wash
B
Throat swab
C
BAL
D
Rectal swab
E
Whole blood
Viral RNA
(cDNA copies/ml)
10^3
10^4
10^5
10^6
10^7
10^8
10^9
1 2 3 4 5 6 8 9 11 12 14 15 18 19
4 5 14 15 18 19
Time post-challenge (Day)

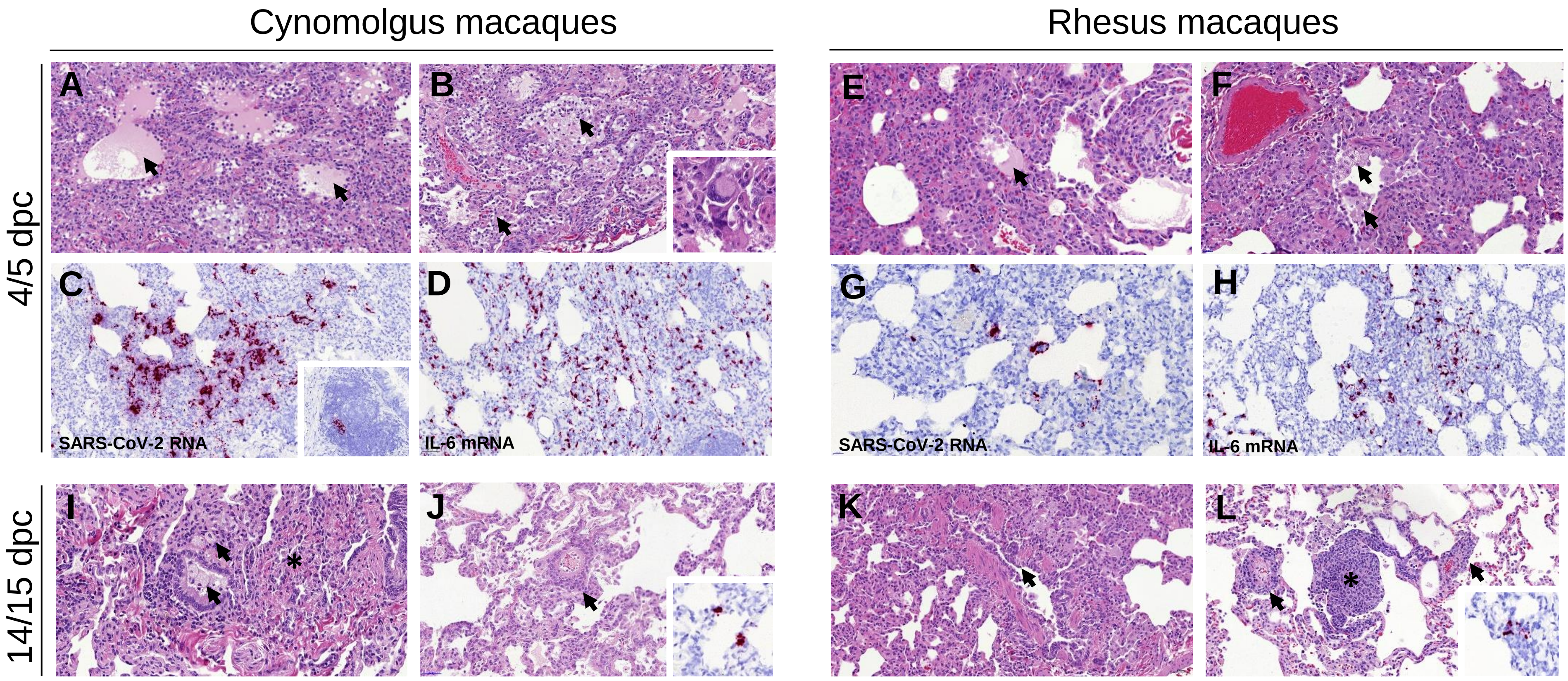
Cynomolgus macaques
Rhesus macaques
4/5 dpc
14/15 dpc
A
B
C
D
E
F
G
H
I
J
K
L
SARS-CoV-2 RNA
IL-6 mRNA
SARS-CoV-2 RNA
IL-6 mRNA
*
*

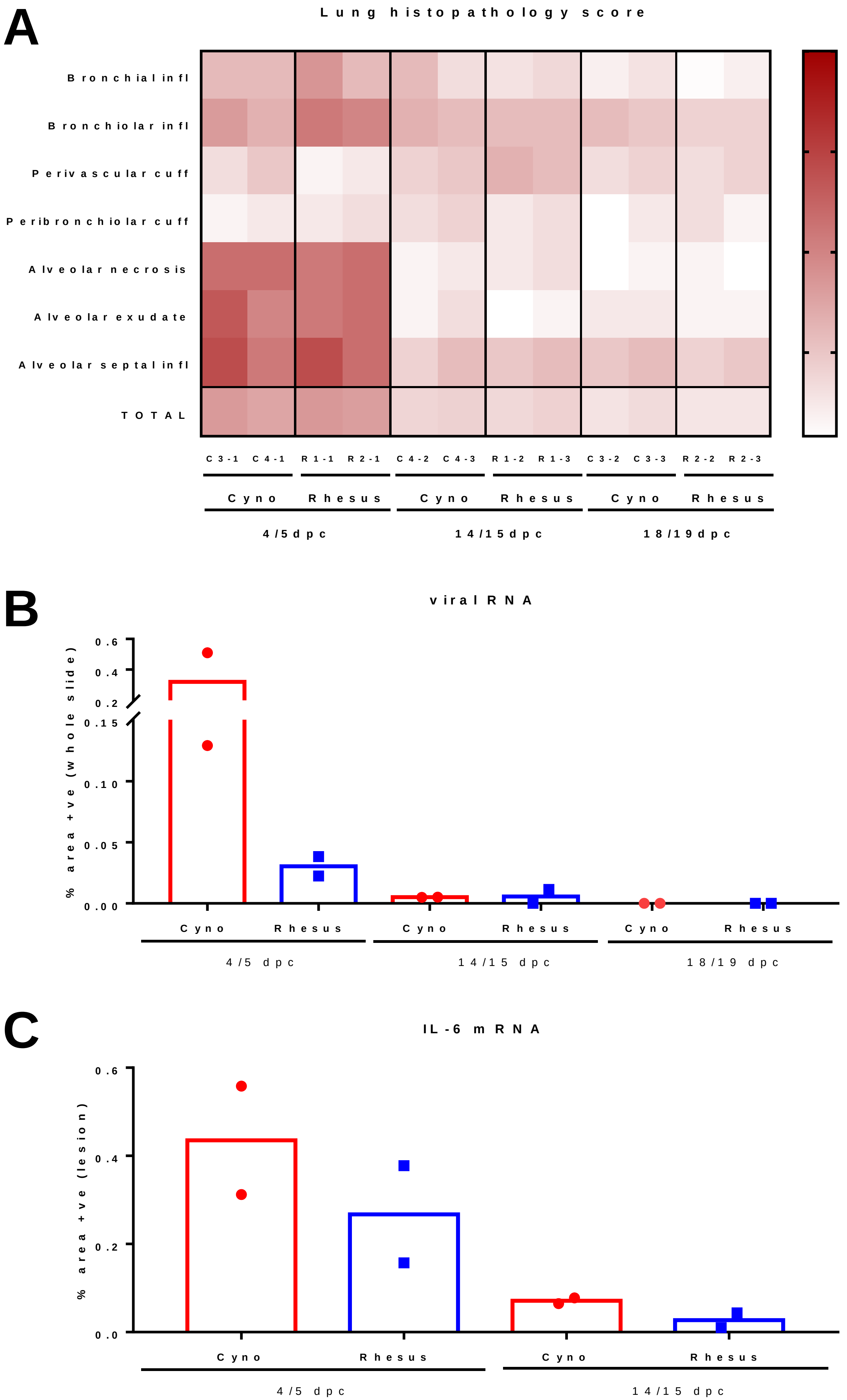
A
Lung histopathology score
Bronchial infl
Bronchiolar infl
Perivascular cuff
Peribronchiolar cuff
Alveolar necrosis
Alveolar exudate
Alveolar septal infl
TOTAL
4
3
2
1
C3-1
C4-1
R1-1
R2-1
C4-2
C4-3
R1-2
R1-3
C3-2
C3-3
R2-2
R2-3
Cyno
Rhesus
Cyno
Rhesus
Cyno
Rhesus
4/5dpc
14/15dpc
18/19dpc
B
viral RNA
% area +ve (whole slide)
0.6
0.4
0.2
0.15
0.10
0.05
0.00
Cyno
Rhesus
Cyno
Rhesus
Cyno
Rhesus
4/5 dpc
14/15 dpc
18/19 dpc
C
IL-6 mRNA
% area +ve (lesion)
0.6
0.4
0.2
0.0
Cyno
Rhesus
Cyno
Rhesus
4/5 dpc
14/15 dpc

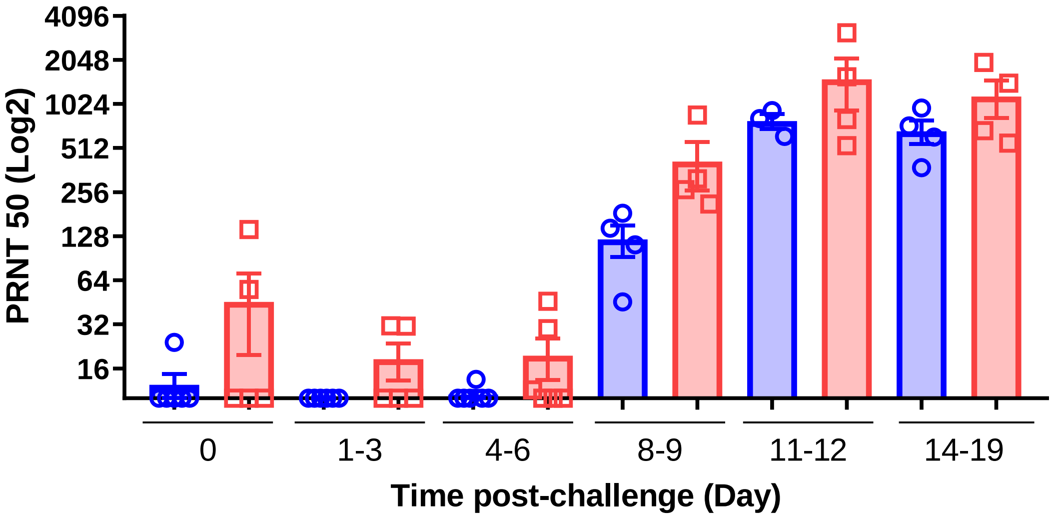
4096
2048
1024
512
256
128
64
32
16
PRNT 50 (Log2)
0
1-3
4-6
8-9
11-12
14-19
Time post-challenge (Day)

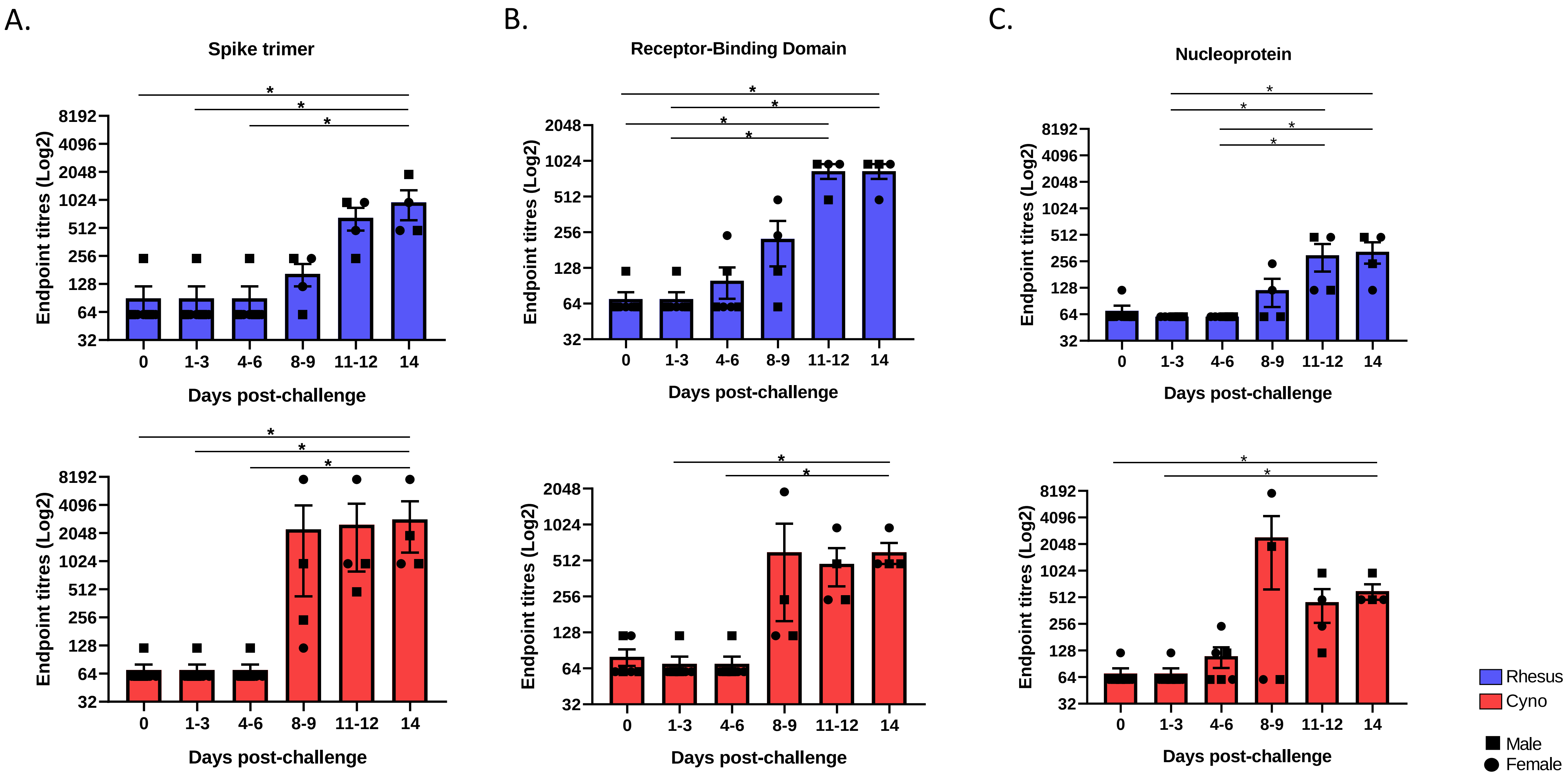
A.
Spike trimer
B.
Receptor-Binding Domain
C.
Nucleoprotein
Endpoint titres (Log2)
8192
4096
2048
1024
512
256
128
64
32
0
1-3
4-6
8-9
11-12
14
Days post-challenge
*
Rhesus
Cyno
Male
Female

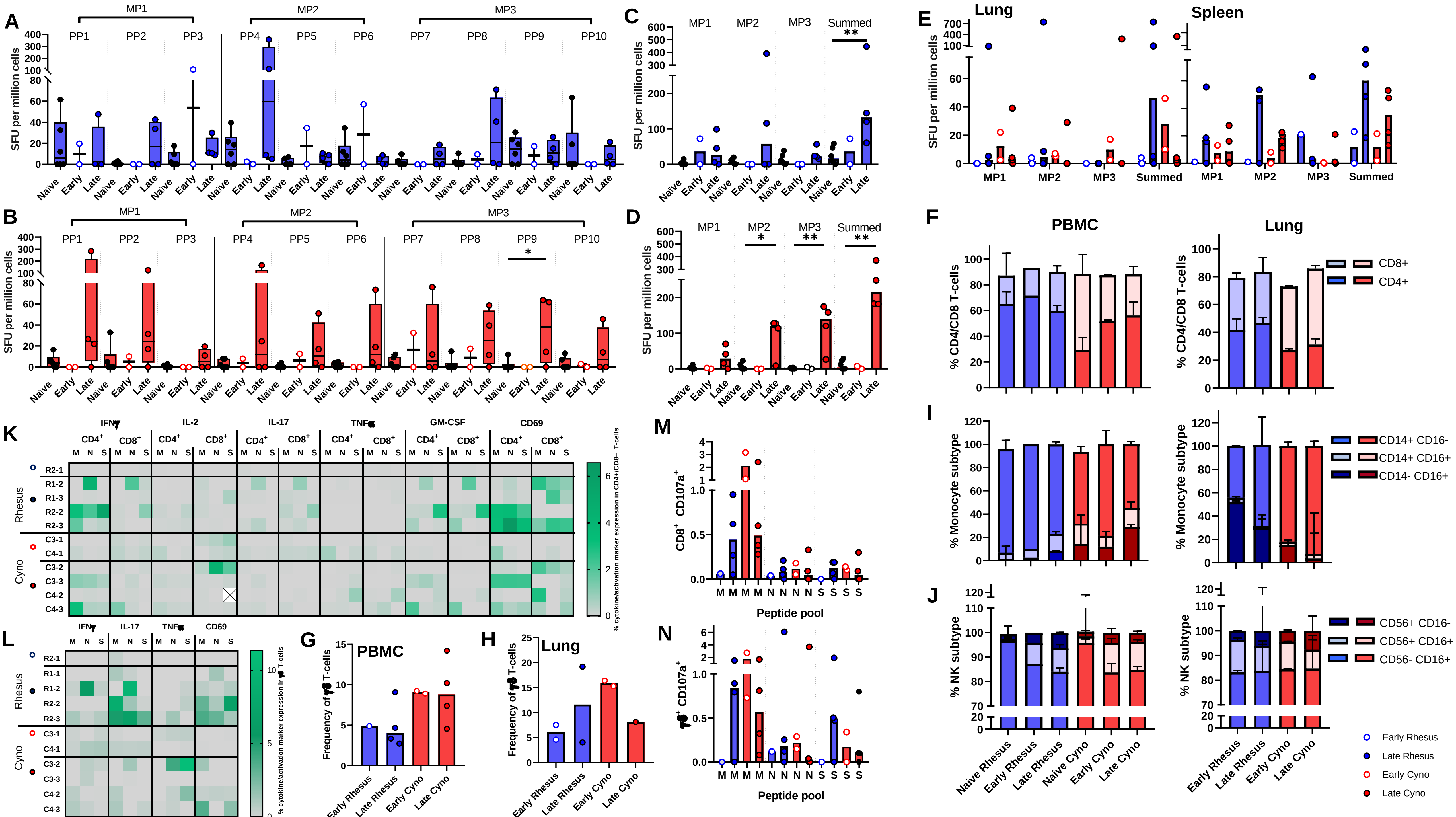
A
MP1
MP2
MP3
PP1
PP2
PP3
PP4
PP5
PP6
PP7
PP8
PP9
PP10
SFU per million cells
Naïve
Early
Late
B
*
C
Summed
**
D
*
**
**
E
Lung
Spleen
F
PBMC
Lung
% CD4/CD8 T-cells
CD8+
CD4+
I
% Monocyte subtype
CD14+ CD16-
CD14+ CD16+
CD14- CD16+
J
% NK subtype
CD56+ CD16-
CD56+ CD16+
CD56- CD16+
Naive Rhesus
Early Rhesus
Late Rhesus
Naive Cyno
Early Cyno
Late Cyno
Early Rhesus
Late Rhesus
Early Cyno
Late Cyno
K
IFNγ
IL-2
IL-17
TNFα
GM-CSF
CD69
$CD4^+$
$CD8^+$
M N S
Rhesus
Cyno
R2-1
R1-2
R1-3
R2-2
R2-3
C3-1
C4-1
C3-2
C3-3
C4-2
C4-3
% cytokine/activation marker expression in CD4+/CD8+ T-cells
L
IFNγ
IL-17
TNFα
CD69
R2-1
R1-1
R1-2
R2-2
R2-3
C3-1
C4-1
C3-2
C3-3
C4-2
C4-3
% cytokine/activation marker expression in γδ T-cells
G
PBMC
Frequency of γδ T-cells
H
Lung
M
$CD8^+$ $CD107a^+$
Peptide pool
N
γδ $CD107a^+$
Peptide pool